npj | computational materials

www.nature.com/npjcompumats

ARTICLE OPEN

In silico screening for As/Se-free ovonic threshold switching materials

Sergiu Clima[1]✉, Daisuke Matsubayashi[2], Taras Ravsher[1,3], Daniele Garbin[1], Romain Delhougne[1], Gouri Sankar Kar[1] and Geoffrey Pourtois[1]

Restricted use of hazardous environmental chemicals is one important challenge that the semiconductor industry needs to face to improve its sustainability. Ovonic threshold switching (OTS) ternary compound materials used in memory selector devices contain As and Se. Engineering these elements out of these materials requires significant research effort. To facilitate this process, we performed systematic material screening for As/Se-free ternary materials, based on ab-initio simulations. To limit the large amount of possible chemical compositions to fewer promising candidates, we used physics-based material parameter filters like material stability, electronic properties, or change in polarizability. The OTS gauge concept is introduced as a computed parameter to estimate the probability of a material to show an OTS behavior. As a result, we identified 35 As/Se-free ternary alloy compositions for stand-alone OTS memory applications, as well as 12 compositions for RRAM selector applications. This work aims seeding the development of As/Se-free OTS materials.

npj Computational Materials (2023)9:96 ; https://doi.org/10.1038/s41524-023-01043-2

INTRODUCTION

Cross-point array with non-volatile resistive random-access-memories (RRAM) such as phase change memories (PCM) is a key technology to achieve high memory capacity and cost efficiency. The performance of this architecture depends upon 2-terminal selector devices set in series with the RRAM cells. It filters the parasitic leakage current on half-biased low-resistance-state memory cells, while allowing the correct reading of a high-resistance-state memory cell. To facilitate its integration with IC systems, the selector materials require to be robust under back-end-of-line (BEOL) integration and the electrical cyclic stress. Several amorphous chalcogenide materials show ovonic threshold switching (OTS)[1]. This is one of the suitable physical mechanisms that can deliver the desired selector properties such that the leakage current through the device is orders of magnitude lower at half of threshold voltage, i.e., leading to high non-linearity[2].

The mainstream OTS materials are generally based on As and Se[3–11], whereas using the materials containing such hazardous chemicals should be avoided as much as possible to minimize their impact on our environment. In this sense, it is crucial to search for As/Se-free OTS materials that meet the performance demands. Extensive device studies have already proposed a set of possible alternative alloys based on Te (B-Te, C-Te, Zn-Te, Ge-Te, Si-Te, Ag-Si-Te, Mg-Te, Ge-C-Te, and Hf-O-Te)[12–22] and S-based system Ge-S[23–25]. However, most of these are facing reliability challenges[26–29] hence more robust materials are needed. Initial results of the ab-initio systematic screening for As/Se-free alloys with good OTS electrical behavior and material stability were presented recently[30]. In this work, we extended and generalized the study to identify OTS material candidates with two target applications in mind, namely “RRAM selector” and “OTS memory”. The latter was recently proposed as a stand-alone self-rectified memory concept[31,32]. More specifically, we focus on identifying ternary compounds and downselect potentially-promising OTS materials using eight screening filters: undesirable/ toxic element exclusion, OTS-compatible electronic configuration (5 valence-electron rule[33,34]), phase stability of the amorphous alloys at BEOL temperatures (high glass-transition temperature), high chemical stability (low formation enthalpy), low leakage current (open trap gap), immunity to phase demixing (low spinodal temperature[35]), application-compatible trap/ mobility gaps, and OTS behavior indicator (OTS gauge). Starting from more than 13,000 candidates, the filtering process yielded 12 material compositions for RRAM selectors and 35 ones for OTS memory applications. In this work, we detail the computational material screening methodology and report the found promising materials. As such, we hope that this will seed works around the design of As/Se-free OTS materials.

RESULTS AND DISCUSSIONS

Material preselection

The motivation in this work is to identify As/Se-free OTS materials from a vast number of chemical compositions by using ab-initio simulations. We proceed by generating multiple amorphous models with relatively large size (300 atoms, ~2 × 2 × 2 nm) and computing the electronic structure with density functional theory (DFT). Because DFT simulations are rather time-consuming, it is impractical to simulate all possible combinations of ternary alloys. For that reason, we reduce the number of compositions to be simulated to a smaller subset of materials that complies with certain known OTS criteria, by applying the three-step screening filters illustrated in Fig. 1a.

The first filter consists in excluding elements to narrow down the number of combinations to be considered (Fig. 1b). We excluded As, Se and Cd since they are known to be toxic. We hence focused on the following 14 elements: B, C, N, Al, Si, P, S, Zn, Ga, Ge, In, Sn, Sb, and Te. All possible ternary combinations of the 14 elements using a 10% atomic fraction step generate 13,104 compositions.

[1]imec, Kapeldreef 75, B-3001 Leuven, Belgium. [2]Device Technology Research & Development Center, Future Memory Development Department, KIOXIA Corporation, Shin-sugita-cho 8, Isogo-ku, Yokohama, Japan. [3]KU Leuven, Celestijnenlaan 200D, B-3001 Leuven, Belgium. ✉email: Sergiu.Clima@imec.be

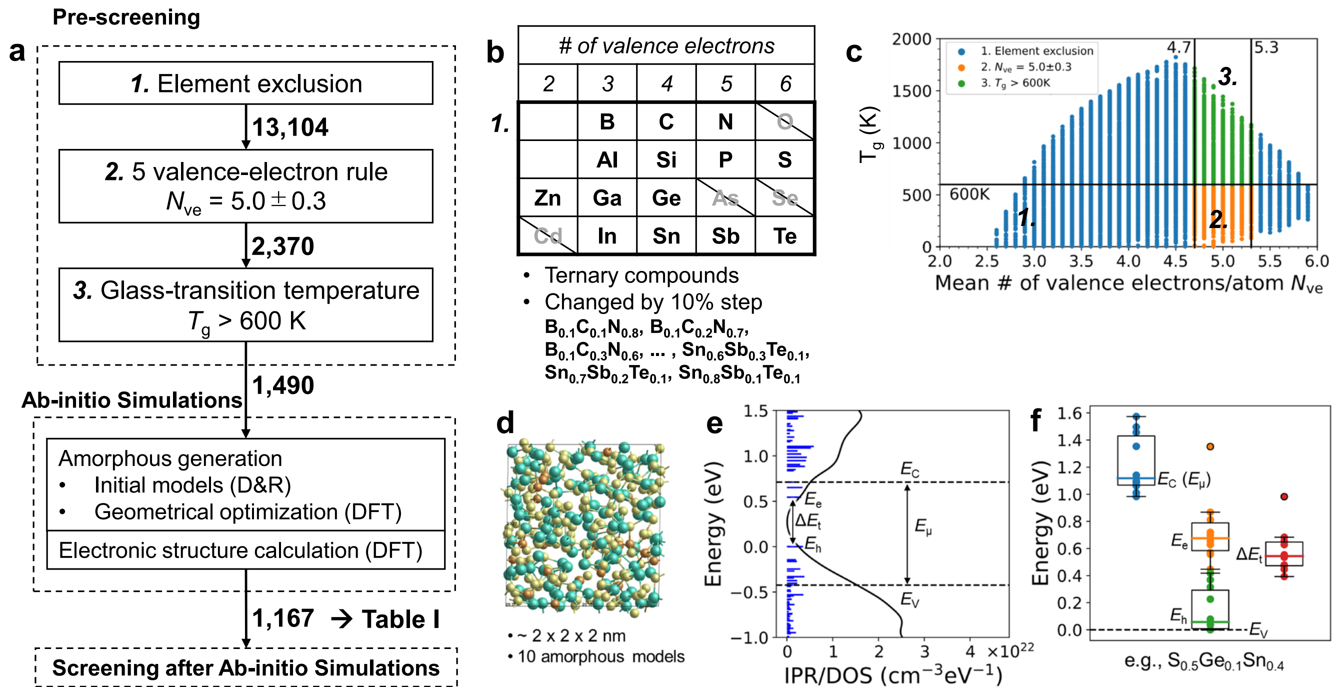

Fig. 1 Material preselection criteria and ab initio simulated electronic structure parameters. a Preselection flowchart for the materials to be simulated with ab-initio. **b** Element and composition selection. **c** Mean number of valence electrons per atom N_{ve} and glass-transition temperature T_g of the compositions on the first, second and third screening steps. **d** Amorphous atomistic model example, generated with ab-initio simulations. **e** Ab-initio gap parameters (mobility gap E_μ, electron / hole trap levels E_e/E_h, and trap gap ΔE_t) extracted using inverse participation ratio (IPR) denoted by discrete lines. **f** Statistics of the gap parameters from 10 amorphous models (boxplots show the quartiles and the median, the whiskers show the range of the data, outliers indicated outside whiskers).

Table 1. Composition reduction in ab-initio simulations.

# of compositions	Description
1490	D&R tried
312	D&R fail
1178	D&R pass → DFT tried
11	≤6 models converged
1167	≥7 models converged
1157	10 models converged
8	9 models converged
1	8 models converged
1	7 models converged

For a second screening filter, the 5 valence-electron rule was used[33,34]. Five valence electrons per atom in amorphous chalcogenides result in populating localized antibonding states, which makes bonding in some regions of the material unstable. This local instability is the key to activate the OTS mechanism, which reflects the transition from insulator to conductor of the material. We found that the mean number of valence electrons per atom (N_{ve}) in the conventional OTS materials, Si-Ge-As-Se, Ge-As-Se, and Si-Ge-As-Te with $N_{ve} \sim 5.0$–5.3 has a good correlation with experimental holding voltage in the metal-OTS-metal devices[30,36]. Accounting for the condition of $N_{ve} = 5.0 \pm 0.3$ extracts 2370 compositions out of the 13,104 ones.

The third filter ensures that the glass-transition temperature (T_g) is higher than 600 K. This condition is expected to distinguish OTS materials from Phase Chance Materials (PCM), since the glass transition temperature is a lower limit of the crystallization temperature. In our understanding, the OTS material should keep its amorphous character during the BEOL processing steps, where a temperature of ~400 °C (673.15 K) is typically applied. However, for the screening condition we applied a larger margin, since the T_g was estimated with the semi-empirical Lankhorst model[37]. This model is applicable to covalent amorphous materials with $N_{ve} \geq 4$ and is expected to be inaccurate for compositions with lower N_{ve}. In the range of interest, $N_{ve} = 5.0 \pm 0.3$, T_g is expected to be more accurate, though it was found to overestimate the T_g for SiGeTe compositions[38]. Figure 1c describes the first, second and third screening steps in terms of N_{ve} and T_g. For the condition of $T_g > 600$ K, 1490 compositions out of the 2370 ones were downselected. As a result, the initial 13,104 compositions were reduced to 1490, which are to be simulated with DFT.

Ab-initio simulations

Our atomistic simulations are divided into two stages as shown in Fig. 1a. The first stage is the generation of 10 different amorphous 300-atom models (Fig. 1d) per composition. In the second stage, we computed accurate electronic structures (Fig. 1e). The process of composition reduction through the ab-initio simulations is summarized in Table 1. For further screening, we applied additional filters to the computed DFT parameters for the 1167 compositions and focused on the median values of 7–10 amorphous models to gain a statistically relevant sampling (Fig. 1f).

Figure 2 shows the element occupancy, which indicates the percentage of the screened compositions containing each element, for each pre-selection step, up to the ab-initio simulations. In the first step of the element exclusion filter, all elements are represented with the same probability. The application of the second filter makes 6 valence electrons elements (S and Te) dominant and the dominance of elements with fewer valence electrons is lowered. There are nine elements with less than 5 valence electrons, whereas there are only two elements with more than 5. As a result, S and Te are appearing

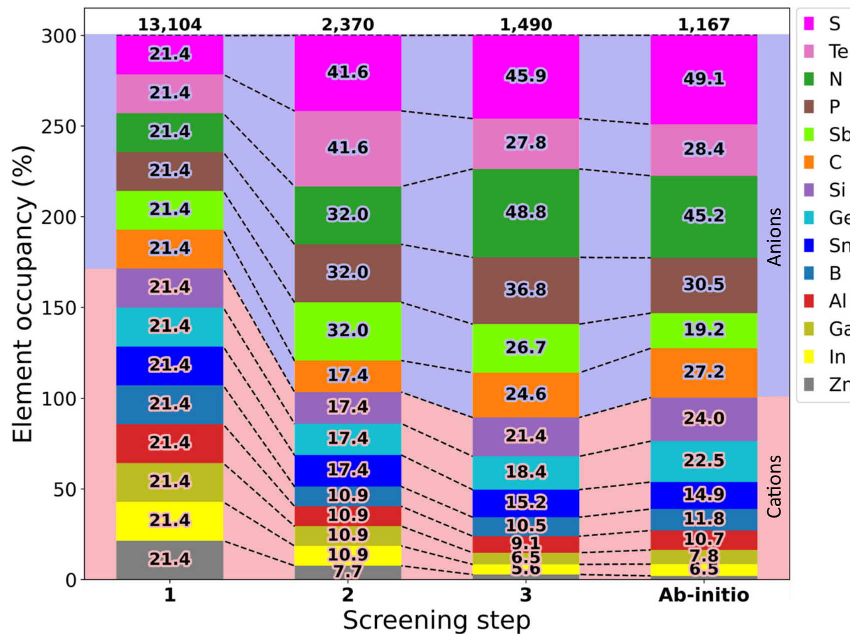

Fig. 2 Element occupancy of the screened compositions for each screening step up to the ab-initio simulations. Note that the maximum of each element occupancy is normalized to 100% and the total of all the element occupancies are 300% due to the ternary nature of the alloys.

more frequently than the other elements to satisfy the 5 valence-electrons-rule. The third filter ($T_g > 600$ K) enhances the contribution of the N element and reduces the Te one. This can be ascribed to stronger, more rigid N, C or Si bonds with higher breaking kinetic barriers[4]. As a result, the contribution of these elements increases, and S and N become the dominant species. This trend is maintained after the ab-initio simulations, and almost half of the 1167 alloys contain S and N.

Figure 3a describes the flowchart of the material screening procedure based on the ab-initio parameters. Applying the remaining 4 filters reduces the initial 1167 candidates to only 35 or 12 ones, for the "OTS memory" or "RRAM selector" target applications, respectively. The details are explained in the following.

Thermodynamic stability and open electronic gap

We introduce two more screening filters to assess the quality of amorphous structures in terms of E_{form} and ΔE_t, which are plotted in Fig. 3b. The fourth filter reflects the negative formation enthalpy ($E_{form} < 0$ eV/atom), which assures the thermodynamic stability of the amorphous structure. In contrast, the amorphous structure with positive E_{form} is thermodynamically unfavorable. Even if such amorphous materials were deposited, they have a high risk of atomic diffusion under thermal or electrical stress[39], leading to reliability issues during the device switching[40]. Therefore, we imposed the condition of $E_{form} < 0$ eV/atom for each composition, which narrowed down the list of candidates to 424 stable ones. Figure 4 shows the element occupancy for the screening steps after the ab-initio simulations. The alloys containing Te, N, Sb, and C tend to be screened out: N-rich materials are not thermodynamically stable (decomposing as N_2 is energetically very favorable) but also their electronic properties indicate higher leakage potential and high potential for phase demixing. Te and Sb are mainly excluded because of their thermodynamic (fourth filter) and demixing (sixth filter) instability. C compounds also have higher preference for C-C bonds[4], which are detrimental to the OFF state of the selector. As a result, S-containing alloys dominate the distribution with a 96.5% occurrence after this filtering step.

The fifth filter relies on the positive trap gap $\Delta E_t > 0$ eV as a proxy indicator for low leakage current. In amorphous materials, although trap levels essentially exist in the mobility gap, the opening of a finite ΔE_t is required, to suppress the leakage current mediated by gap states and therefore to switch-off the OTS device. Otherwise, the overlapping electron-hole traps will show high probability for the electrons to hop or tunnel and result in high leakage current[41]. The condition of $\Delta E_t > 0$ eV further downselected only 360 compositions out of the 424 ones. The element occupancy is almost unchanged except for a slight decrease of the N case, as illustrated in Fig. 4.

Phase stability

To assess the dynamic phase stability against demixing into more stable constituent components of the remaining 360 compositions, we estimated the spinodal temperature $T_{spinodal}$[35]. This concept implies that if a given-temperature T is higher than the $T_{spinodal}$ one, the resulting mixing entropy will stabilize the alloy structure. However, if $T < T_{spinodal}$, the stability brought by the mixing entropy would not be large enough to stabilize the alloy, which can subsequently demix into more stable sub-compositions. Therefore, $T_{spinodal}$ is desired to be as low as possible to promote the alloying stability. For example, $S_{0.5}Ge_{0.1}Sn_{0.4}$, one of the candidate compositions, is surrounded by SnS, $SnGeS_3$, and Ge on the computed (crystalline) phase diagram of the S-Ge-Sn[42]. This indicates that $S_{0.5}Ge_{0.1}Sn_{0.4}$ could demix into these three phase-stable compositions at $T < T_{spinodal}$.

To estimate $T_{spinodal}$ of this alloy, we calculated the second derivative (curvature) of the Gibbs free energy G_{mix} (or E_{form}) around the composition on the phase diagram, as formalized in Supplementary Note 1. Since the data points (generated compositions) on the phase diagram were insufficient to calculate properly the curvature, we trained a machine learning (ML) prediction model of amorphous E_{form} for any arbitrary compositions. For that, we mapped each composition to a 14-dimensional vector (e.g. $S_{0.5}Ge_{0.1}Sn_{0.4}$ to [0, 0, 0, 0, 0, 0, 0.5, 0, 0, 0.1, 0, 0.4, 0, 0]) and used support vector regression with cubic poly-nominal using scikit-learn[43,44]. The ML E_{form} dataset contained 12,357 datapoints

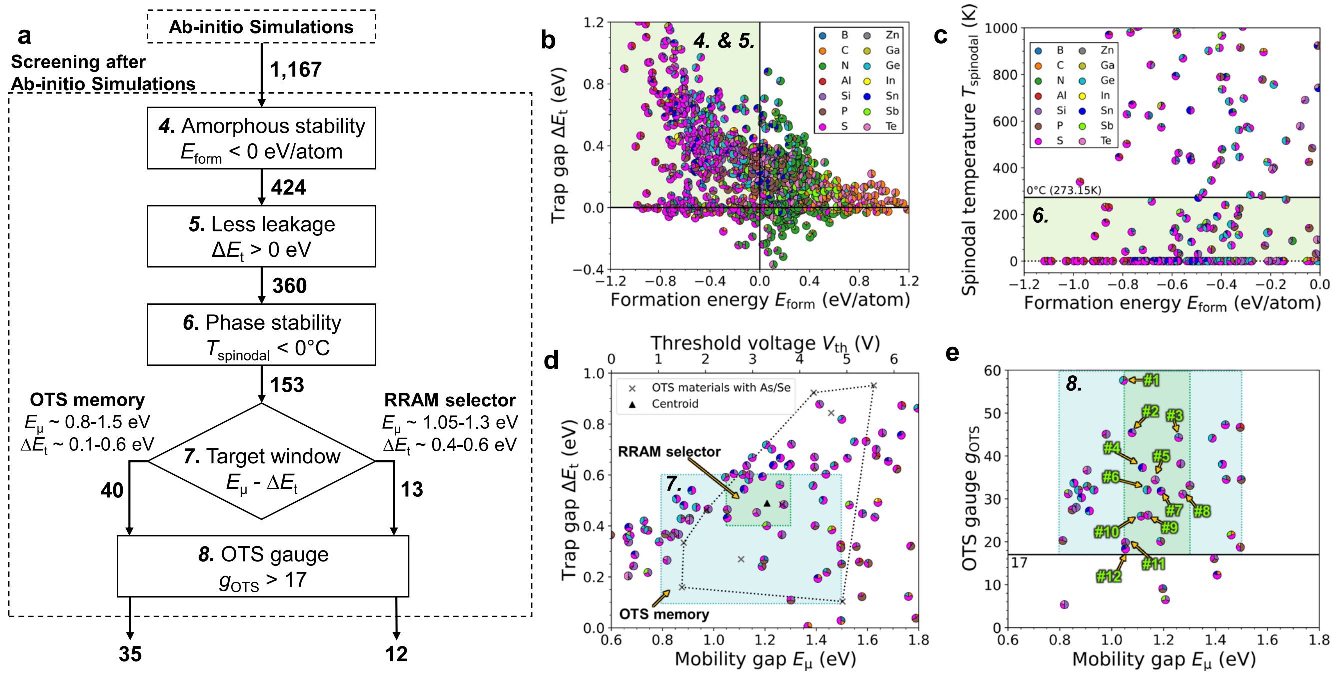

Fig. 3 Material selection criteria on ab-initio simulated data. **a** Flowchart of the screening process based on the results of the DFT simulations. **b** Formation enthalpy E_{form} and trap gap ΔE_t of the compositions on the fourth and fifth screening steps. The symbol of each ternary composition is depicted as a pie chart whose occupation reflects the element fractions. The compositions within the shaded region are selected. **c** E_{form} and spinodal temperature $T_{spinodal}$ of the compositions on the sixth screening step. **d** Mobility gap E_μ and ΔE_t of the compositions on the seventh screening step. The upper x-axis maps the threshold voltage from the correlation between the ab-initio E_μ and the experimental data of the existing 20 nm thick OTS materials with As/Se, denoted by cross markers. The closed triangle marker depicts the centroid of the cross markers. **e** E_μ and OTS gauge g_{OTS} of the compositions on the eighth screening step. #1–12 are the compositions suitable for RRAM selectors.

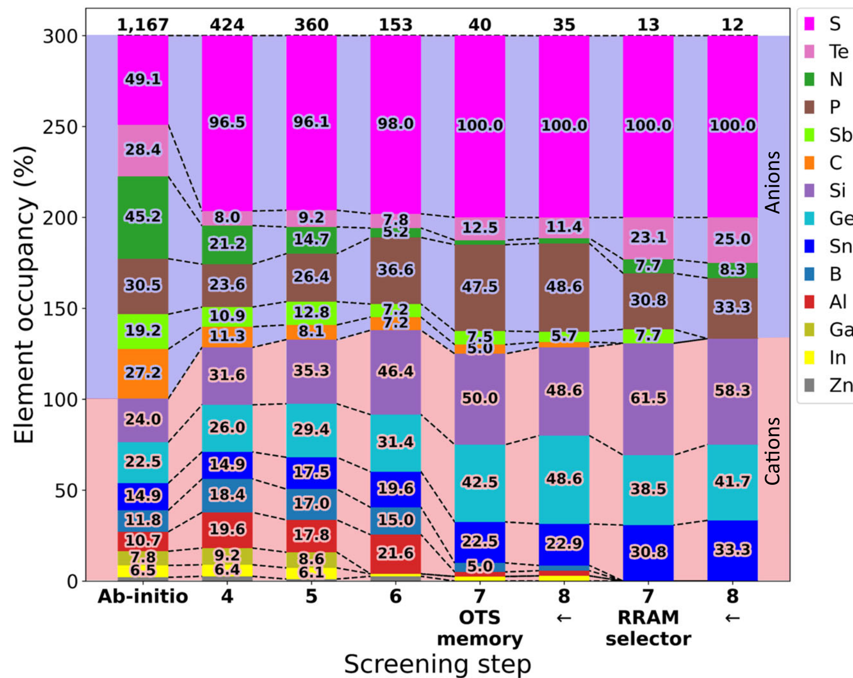

Fig. 4 Element occupancy of the screened compositions for the screening steps after the ab-initio simulations. Note that the maximum of each element occupancy is normalized to 100% and the total of all the element occupancies are 300% due to the ternary nature of the alloys.

consisting of 1167 ternary screened compositions (11,657 amorphous models), 28 ternary/binary convex-hull compositions originally not included in the screening set (28 × 10 different amorphous models) and 14 single-element materials (with formation enthalpy set to zero). 90% of the dataset was used for the training step and 10% for testing. As a result, the E_{form} prediction model reproduced the original data very well: $R^2 = 0.9784$ for testing data and a mean absolute error of

0.034 eV/atom, only slightly higher than the variation (std = 0.022 eV/atom) of the E_{form} of the amorphous models.

We evaluated $T_{spinodal}$ of the 366 compositions using the E_{form} prediction model (Fig. 3c). Many of the compositions including $S_{0.5}Ge_{0.1}Sn_{0.4}$ were predicted to have $T_{spinodal} = 0$ K, i.e., they are expected to be stable against demixing at any temperature. Since typically the deposition temperature of OTS materials is higher than the room temperature, we imposed $T_{spinodal} < 0$ °C (273.15 K) as the sixth screening filter, which downselected 153 phase-stable compositions out of the 360 ones. According to Fig. 4, P and Si-occupancies remarkably increase and N-occupancy further decreases. In addition, Ga-containing compositions disappear at this point.

Target gap-trap window

For the seventh screening filter, we tuned the expectation windows of E_μ and ΔE_t based on the targeted applications for the OTS materials. In As/Se-based OTS materials, we identified strong correlations between the computed E_μ and experimental electrical parameters such as threshold voltage V_{th}, first-fire voltage V_{ff}, and leakage current I_{leak}[30,36]. Besides, charge excitation from a hole trap level to an electron one induced by an external electric field is a precursor step to switch-on OTS devices[45,46]. In line with this observation, ΔE_t has a correlation with the experimental parameters as well as E_μ[15]. This means that large E_μ or ΔE_t induces high V_{th} and low I_{leak}. Therefore, an optimal range of E_μ and ΔE_t should be defined based on the targeted application.

In this work, we considered two types of applications, "OTS memory" and "RRAM Selector", as shown in Fig. 3d. In line with the stand-alone OTS memory that was recently proposed[32], we took a relatively large target window for the operation of the "OTS memory": $E_\mu \sim 0.8$–1.5 eV/$\Delta E_t \sim 0.1$–0.6 eV, corresponding to $V_{th} \sim 1$–5 V as mapped from the correlation in the existing OTS materials with As/Se. This window filter yields 40 S-based compositions out of the 153 ones. Aside from S, they mainly consist of P, Si, Ge, Sn or Te, and can include small amounts of N, Sb, C, B, Al, or In. No Zn-containing compositions are included (Fig. 4).

A second, smaller target window was defined for "RRAM selector" as $E_\mu \sim 1.05$–1.3 eV/$\Delta E_t \sim 0.4$–0.6 eV, corresponding to $V_{th} \sim 2.5$–3.8 V. This window isolated 13 S-based compositions out of the previous 35 and excludes the alloys with C, B, Al, In and Zn.

OTS gauge

The final (eighth) screening filter that we used (the OTS gauge), consists of assessing the probability of the material candidate to exhibit good OTS behavior. We defined the OTS gauge based on the Born effective charges Z^*, which are also known as dynamic charges and describe the electrical polarization induced by a small displacement of each atom. It has been shown that in amorphous OTS materials, electronic excitation largely increases the number of Z^* at the atoms with a conductive bonding structure[45]. In this work, we used an electronic charge injection in an atomic model instead of an electronic excitation and defined the OTS gauge g_{OTS} as being the "change induced in the total Born effective charges by unit system charge injection" as formulated in Supplementary Note 2.

In a previous report[30], we calculated the OTS gauges for a set of existing OTS materials (Si-Ge-As-Se with 2 different compositions, Ge-As-Se with 3 different compositions, GeSe, Si-Ge-As-Te with 4 different compositions, and SiTe) and non-OTS insulator materials as reference (c-AlN, c-Al_2O_3, c-HfO_2, c-SiO_2). The existing OTS materials had relatively large values (17–62) compared to the non-OTS ones (1–2)[30]. In addition, the OTS gauges had a strong positive correlation with the experimental holding currents[30,36], which corresponds to the minimum value of the on-state currents in the OTS devices. This finding indicates that the Z^*-based OTS gauge can reasonably reflects the physics of the on-state in the OTS device, even though the Z^* are typically a property reflecting the insulative character of the system.

With the validity of the OTS gauge as a quantitative OTS indicator being confirmed on non-OTS materials, we applied it as a funneling parameter to the remaining 40 OTS candidates for the OTS memory (Fig. 3e). The computed OTS gauges spanned in the 5–58 range and only 6 compositions had smaller values than $g_{OTS} = 17$, the lower limit of known OTS materials[36]. Therefore, we set the eighth screening filter at $g_{OTS} > 17$, which yields 35 compositions out of 41 as suitable OTS memory materials. For RRAM selector materials, only 12 compositions out of 13 have suitable OTS gauge (#1–12 in Fig. 3e) and only the Sb-containing composition was excluded.

Analysis of the identified candidates

The screened As/Se-free ternary compositions for OTS memory after the eighth screening filter are summarized in Table 2. The numbers (#1–12) in the RRAM column denote the 12 RRAM selector candidates ordered by the OTS gauge values. Remarkably, all the 35 compositions contain S.

Figure 5 shows the spinodal temperature profiles of the 12 S-based ternary systems including the 35 candidates. In general, S > ~40% composition regions tend to be phase-stable ($T_{spinodal} < 0$ °C), except (b) C-S-Sb and (c) N-S-Sn systems where C or N > ~20% regions tend to be unstable. On the profiles, we also plotted the compositions either within or outside the target windows of "RRAM selector" and "OTS memory". It is worth mentioning that for the (a) B-P-S, (b) C-N-Sb, (c) N-S-Sn, (h) Si-S-Sb, and (k) P-S-In systems, there are few stable compositions. However, these fall out of the defined windows for RRAM selector / OTS memory. Within the selected windows, the compositions satisfy $T_{spinodal} < 0$ °C and OTS gauge > 17, with an optimal ratio of S that ranges from 30% to 60%.

From these profiles, we evaluated the robustness of each candidate against phase demixing by calculating the minimum composition change to the line of $T_{spinodal} = 0$ °C, which was defined as a "composition change margin" in the Table 2. Some of the OTS memory candidates ($B_{0.2}P_{0.5}S_{0.3}$, $C_{0.2}S_{0.5}Sb_{0.3}$, $Si_{0.3}P_{0.4}S_{0.3}$, $Si_{0.1}S_{0.4}Ge_{0.5}$, $P_{0.2}S_{0.3}Ge_{0.5}$, $P_{0.5}S_{0.4}In_{0.1}$, and $S_{0.6}Ge_{0.3}Sn_{0.1}$) have a margin lower than 5.0%. For the 12 RRAM selector candidates, the margins of $Si_{0.4}S_{0.3}Te_{0.3}$ (#5) and $N_{0.1}S_{0.6}Sn_{0.3}$ (#12) raise slightly to 8.6% and 6.3%, respectively. The other 10 alloys have a 10.0% (or more) and are promising. Out of these, 4 materials (#1, 6, 10, and 11) contain a combination of P and S. Unfortunately, they would turn out to be challenging to use in a mass-production product, since the P-S compounds are known as easily flammable solids[47] and H_2S is generated by reacting with water. Considering the aforementioned, the remaining 6 compositions (#2, 3, 4, 7, 8, and 9) can be considered as interesting OTS candidates to be developed experimentally.

To summarize, we performed an ab-initio systematic screening for As/Se-free OTS materials, applying eight physics-based OTS screening filters: element exclusions, $N_{ve} = 5.0 \pm 0.3$ valence-electron rule, $T_g > 600$ K, $E_{form} < 0$ eV/atom, $\Delta E_t > 0$ eV, $T_{spinodal} < 0$ °C, E_μ - ΔE_t target windows, and $g_{OTS} > 17$. Through these filters, we identified 35 S-based ternary compositions suitable for OTS memory, out of which only 12 compositions are expected to deliver good properties for a RRAM selector. Taking the manufacturability aspects into account, our simulations suggest that only the materials $Si_{0.3}S_{0.5}Ge_{0.2}$ (#3), $Si_{0.3\text{-}0.2}S_{0.5}Sn_{0.2\text{-}0.3}$ (#2,7), $Si_{0.5\text{-}0.4}S_{0.4}Te_{0.1\text{-}0.2}$ (#8,9), and $S_{0.5}Ge_{0.1}Sn_{0.4}$ (#4) would be interesting to be experimentally investigated.

Table 2. As/Se-free OTS candidate compositions.

	Composition	Composition system	OTS gauge	$T_{spinodal}$ (K)	Composition change margin (%)	E_μ (eV)	ΔE_t (eV)	E_{form} (eV/atom)	T_g (K)	N_{ve}	RRAM
1	$B_{0.2}P_{0.5}S_{0.3}$	B-P-S	34	195	3.8	1.50	0.25	−0.33	752	4.9	
2	$C_{0.2}S_{0.5}Sb_{0.3}$	C-S-Sb	22	0	4.2	1.46	0.38	−0.05	695	5.3	
3	$N_{0.1}S_{0.6}Sn_{0.3}$	N-S-Sn	18	0	6.3	1.05	0.43	−0.49	800	5.3	#12
4	$Al_{0.3}P_{0.4}S_{0.3}$	Al-P-S	47	0	11.3	1.50	0.33	−0.59	685	4.7	
5	$Si_{0.3}P_{0.4}S_{0.3}$	Si-P-S	33	0	10.2	1.30	0.11	−0.37	874	5.0	
6	$Si_{0.3}P_{0.5}S_{0.2}$	↑	20	66	2.9	0.81	0.37	−0.22	878	4.9	
7	$Si_{0.4}P_{0.3}S_{0.3}$	↑	20	0	11.5	1.05	0.46	−0.34	913	4.9	#11
8	$Si_{0.4}P_{0.4}S_{0.2}$	↑	27	0	8.2	0.85	0.37	−0.20	920	4.8	
9	$Si_{0.5}P_{0.1}S_{0.4}$	↑	38	0	11.0	1.27	0.37	−0.48	930	4.9	
10	$Si_{0.5}P_{0.2}S_{0.3}$	↑	45	0	6.1	0.98	0.47	−0.34	936	4.8	
11	$Si_{0.1}S_{0.4}Ge_{0.5}$	Si-S-Ge	32	158	1.2	0.93	0.47	−0.36	800	4.8	
12	$Si_{0.2}S_{0.6}Ge_{0.2}$	↑	47	0	20.0	1.44	0.60	−0.61	823	5.2	
13	$Si_{0.3}S_{0.5}Ge_{0.2}$	↑	44	0	12.7	1.26	0.56	−0.57	871	5.0	#3
14	$Si_{0.5}S_{0.4}Ge_{0.1}$	↑	28	0	7.7	0.86	0.37	−0.45	927	4.8	
15	$Si_{0.2}S_{0.5}Sn_{0.3}$	Si-S-Sn	32	0	10.3	1.19	0.59	−0.67	768	5.0	#7
16	$Si_{0.3}S_{0.5}Sn_{0.2}$	↑	45	0	12.5	1.08	0.61	−0.68	823	5.0	#2
17	$Si_{0.4}S_{0.4}Sb_{0.2}$	Si-S-Sb	31	0	10.0	0.83	0.36	−0.51	828	5.0	
18	$Si_{0.4}S_{0.3}Te_{0.3}$	Si-S-Te	34	0	8.6	1.17	0.45	−0.37	728	5.2	#5
19	$Si_{0.4}S_{0.4}Te_{0.2}$	↑	31	0	17.7	1.27	0.48	−0.53	784	5.2	#8
20	$Si_{0.5}S_{0.2}Te_{0.3}$	↑	37	0	6.8	0.91	0.42	−0.21	757	5.0	
21	$Si_{0.5}S_{0.4}Te_{0.1}$	↑	26	0	12.6	1.14	0.60	−0.52	868	5.0	#9
22	$P_{0.1}S_{0.4}Ge_{0.5}$	P-S-Ge	32	0	10.9	1.14	0.58	−0.38	734	4.9	#6
23	$P_{0.1}S_{0.5}Ge_{0.4}$	↑	44	0	20.8	1.39	0.56	−0.52	722	5.1	
24	$P_{0.2}S_{0.3}Ge_{0.5}$	↑	32	0	4.6	0.87	0.43	−0.28	724	4.8	
25	$P_{0.2}S_{0.4}Ge_{0.4}$	↑	58	0	14.5	1.05	0.59	−0.41	712	5.0	#1
26	$P_{0.3}S_{0.4}Ge_{0.3}$	↑	26	0	15.2	1.11	0.60	−0.40	698	5.1	#10
27	$P_{0.3}S_{0.5}Ge_{0.2}$	↑	35	0	18.5	1.44	0.22	−0.46	680	5.3	
28	$P_{0.4}S_{0.3}Ge_{0.3}$	↑	33	0	5.2	0.91	0.43	−0.28	722	5.0	
29	$P_{0.4}S_{0.4}Ge_{0.2}$	↑	20	0	9.8	1.19	0.24	−0.36	697	5.2	
30	$P_{0.5}S_{0.4}In_{0.1}$	P-S-In	19	49	3.7	1.50	0.31	−0.44	603	5.2	
31	$S_{0.5}Ge_{0.1}Sn_{0.4}$	S-Ge-Sn	37	0	19.2	1.12	0.54	−0.62	662	5.0	#4
32	$S_{0.5}Ge_{0.2}Sn_{0.3}$	↑	27	0	16.0	0.91	0.54	−0.58	677	5.0	
33	$S_{0.5}Ge_{0.3}Sn_{0.2}$	↑	30	82	13.0	0.88	0.48	−0.52	697	5.0	
34	$S_{0.5}Ge_{0.4}Sn_{0.1}$	↑	34	142	12.2	0.85	0.51	−0.46	721	5.0	
35	$S_{0.6}Ge_{0.3}Sn_{0.1}$	↑	38	183	4.4	1.43	0.50	−0.54	709	5.2	

METHODS

Ab-initio simulations

The initial amorphous models were generated by a decorate-and-relax (D&R) algorithm[48]. Each model is a 300-atom system with a ~2 × 2 × 2-nm unit cell (Fig. 1d). The D&R was applied to the pre-selected 1490 compositions. However, the amorphous generations of 312 compositions failed. Starting from the 10 × 1178 initial models obtained by the D&R, we performed geometrical optimization based on density functional theory (DFT) using CP2K software[49]. We used GGA-PBE exchange-correlation functional[50], GTH pseudo-potentials[51] to describe the core electrons, a double-zeta-valence-polarization (DZVP) localized basis sets for the valence electrons and planewaves with a cutoff of 500 Ry and a relative cutoff of 40 Ry were used for the real space integration grid. The Brillouin zone sampling was limited to the Γ-point only. The atomic forces were relaxed with a convergence criterium of 1E-4 Ha/bohr, whereas the pressure was considered converged when below 100 bar. Few compositions faced numerical convergence issues and had less than six atomic models converged, which were excluded from our analysis. As a result, we neglected 11 compositions and used the remaining 1167 ones in the following analysis to consider the statistical behavior of the amorphous models.

The accurate electronic structures were computed using the hybrid exchange-correlation functional (HSE06) in combination with the auxiliary density matrix method (ADMM)[52]. The hybrid functional and large enough atomic model size will ensure a better detection of the traps in the gap and quantitative accuracy of the mobility gaps[53]. For the mobility gap estimation, we used the inverse participation ratio (IPR[53]) to identify the mobility edges of the amorphous models shown in Fig. 1e. The mobility gap (E_μ) was taken as the energy difference between the conduction and valence mobility edges (E_C and E_V). The electron and hole trap levels (E_e and E_h) were extracted as the deepest levels with respect to conduction and valence bands, respectively. The trap gap ΔE_t was taken as the energy difference of E_e and E_h. The formation enthalpy per atom (E_{form}) of each amorphous model was

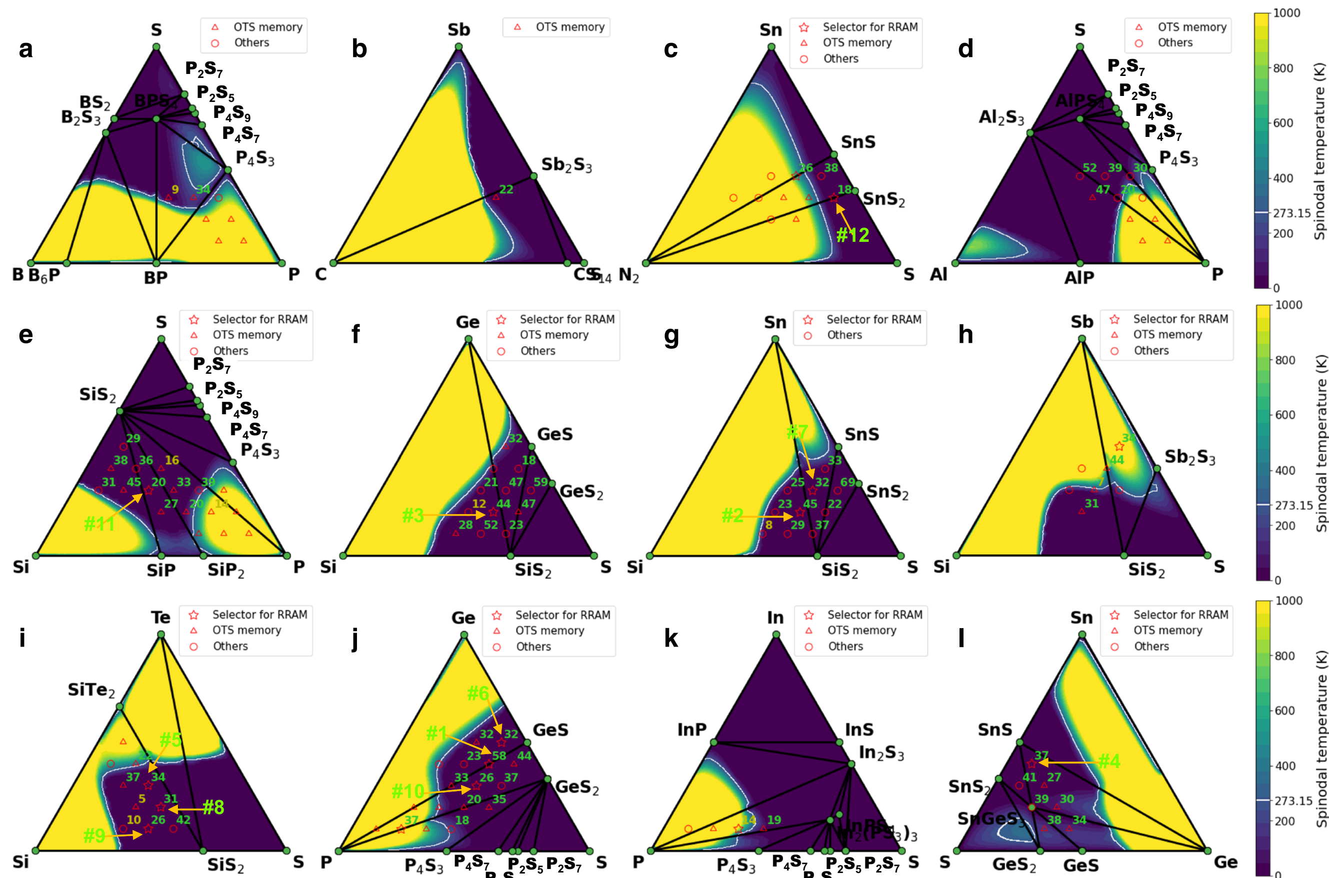

Fig. 5 Spinodal temperature profiles on the ternary phase diagrams. **a** B-P-S, **b** C-S-Sb, **c** N-S-Sn, **d** Al-P-S, **e** Si-P-S, **f** Si-S-Ge, **g** Si-S-Sn, **h** Si-S-Sb, **i** Si-S-Te, **j** P-S-Ge, **k** P-S-In, and **l** S-Ge-Sn. White line shows $T_{spinodal} = 0\,°C$ (273.15 K). The star/# and triangle markers depict the compositions in the targe windows of RRAM selector and OTS memory. Circle markers depict the compositions outside the target windows but within $E_\mu \sim 0.6–1.8$ eV/$\Delta E_t \sim 0.0–1.0$ eV. The numbers beside the markers indicate the OTS gauge values.

predicted with the materials graph network (MEGNet) model[54], which is based on machine learning trained on the Materials Projects dataset[55].

DATA AVAILABILITY

Data related to this work are available upon reasonable request.

CODE AVAILABILITY

The codes that support the findings of this study are available upon reasonable request.

Received: 31 January 2023; Accepted: 8 May 2023;
Published online: 03 June 2023

REFERENCES

1. Ovshinsky, S. R. Reversible electrical switching phenomena in disordered structures. *Phys. Rev. Lett.* **21**, 1450–1453 (1968).
2. Burr, G. W. et al. Access devices for 3D crosspoint memory. *J. Vac. Sci. Technol. B* **32**, 040802 (2014).
3. Cheng, H. Y. et al. An ultra high endurance and thermally stable selector based on TeAsGeSiSe chalcogenides compatible with BEOL IC Integration for cross-point PCM. In *2017 IEEE International Electron Devices Meeting (IEDM)* 2.2.1–2.2.4 (IEEE, 2017).
4. Clima, S. et al., Atomistic investigation of the electronic structure, thermal properties and conduction defects in Ge-rich GexSe1−x materials for selector applications. In *2017 IEEE International Electron Devices Meeting (IEDM)* 4.1.1–4.1.4 (IEEE, 2017).
5. Govoreanu, B. et al. Thermally stable integrated Se-based OTS selectors with >20 MA/cm 2 current drive, >3.10 3 half-bias nonlinearity, tunable threshold voltage and excellent endurance. In *2017 Symposium on VLSI Technology* T92–T93 (IEEE, 2017).
6. Cheng, H. Y. et al. Ultra-high endurance and low IOFF selector based on AsSeGe chalcogenides for wide memory window 3D stackable crosspoint memory. In *2018 IEEE International Electron Devices Meeting (IEDM)* 37.3.1–37.3.4 (IEEE, 2018).
7. Garbin, D. et al. Composition optimization and device understanding of Si-Ge-As-Te ovonic threshold switch selector with excellent endurance. In *2019 IEEE International Electron Devices Meeting (IEDM)* 35.1.1–35.1.4 (IEEE, 2019).
8. Kabuyanagi, S. et al. Understanding of tunable selector performance in Si-Ge-As-Se OTS devices by extended percolation cluster model considering operation scheme and material design. In *2020 IEEE Symposium on VLSI Technology* 1–2 (IEEE, 2020).
9. Cheng, H. Y. et al. Optimizing AsSeGe chalcogenides by dopants for extremely low I_{OFF}, high endurance and low V_{th} drift 3D crosspoint memory. In *2021 IEEE International Electron Devices Meeting (IEDM)* 28.6.1–28.6.4 (IEEE, 2021).
10. Cheng, H. Y. et al. New phase-change materials by atomic-level engineering the dopants for extremely low V_{th} drift at 85 °C and high endurance 3d crosspoint memory: IBM/Macronix PCRAM joint project. In *2022 International Electron Devices Meeting (IEDM)* 18.5.1–18.5.4 (IEEE, 2022).
11. Gu, R. et al. How arsenic makes amorphous GeSe a robust chalcogenide glass for advanced memory integration. *Scr. Mater.* **218**, 114834 (2022).
12. Yoo, J., Lee, D., Park, J., Song, J. & Hwang, H. Steep slope field-effect transistors with B–Te-based ovonic threshold switch device. *IEEE J. Electron Devices Soc.* **6**, 821–824 (2018).
13. Chekol, S. A. et al. A C–Te-based binary OTS device exhibiting excellent performance and high thermal stability for selector application. *Nanotechnology* **29**, 345202 (2018).
14. Koo, Y. & Hwang, H. Zn1−xTex ovonic threshold switching device performance and its correlation to material parameters. *Sci. Rep.* **8**, 11822 (2018).
15. Anbarasu, M., Wimmer, M., Bruns, G., Salinga, M. & Wuttig, M. Nanosecond threshold switching of $GeTe_6$ cells and their potential as selector devices. *Appl. Phys. Lett.* **100**, 143505 (2012).

16. Yunmo Koo, Kyungjoon Baek, & Hyunsang Hwang. Te-based amorphous binary OTS device with excellent selector characteristics for x-point memory applications. In *2016 IEEE Symposium on VLSI Technology* 1–2 (IEEE, 2016).
17. Song, B., Xu, H., Liu, S., Liu, H. & Li, Q. Threshold switching behavior of Ag-SiTe-based selector device and annealing effect on its characteristics. *IEEE J. Electron Devices Soc.* **6**, 674–679 (2018).
18. Lee, S., Lee, J., Kim, S., Lee, D. & Hwang, H. Mg-Te OTS selector with Low Ioff (< 100 pA), Fast Switching Speed (τd = 7 ns), and High Thermal Stability (400 °C / 30 min) for X-point Memory Applications. In *2021 Symposium on VLSI Technology*. 1-2 (IEEE, 2021).
19. Wu, C.H. et al. Low-voltage (~1.3V), arsenic free threshold type selector with ultra high endurance (> 1011) for high density 1S1R memory array. In *2021 Symposium on VLSI Technology* 1-2 (IEEE, 2021).
20. Ambrosi, E. et al. Low variability high endurance and low voltage arsenic-free selectors based on GeCTe. In *2021 IEEE International Electron Devices Meeting (IEDM)* 28.5.1–28.5.4 (IEEE, 2021).
21. Hatayama, S., Saito, Y. & Uchida, N. Amorphous Hf–O–Te as a selector via a modified conduction mechanism by Te content control. *APL Mater.* **10**, 011106 (2022).
22. Gu, R. et al. Structural features of chalcogenide glass SiTe: an ovonic threshold switching material. *APL Mater.* **9**, 081101 (2021).
23. Jia, S. et al. Ultrahigh drive current and large selectivity in GeS selector. *Nat. Commun.* **11**, 4636 (2020).
24. Kim, M. et al. PE-ALD of $Ge_{1-x}S_x$ amorphous chalcogenide alloys for OTS applications. *J. Mater. Chem. C.* **9**, 6006–6013 (2021).
25. Jia, S., Li, H., Liu, Q., Song, Z. & Zhu, M. Scalability of sulfur-based ovonic threshold selectors for 3D stackable memory applications. *Phys. Status Solidi RRL* **15**, 2100084 (2021).
26. Zuo, W. et al. Volatile threshold switching memristor: an emerging enabler in the AIoT era. *J. Semicond.* **44**, 053102–053123 (2023).
27. Seong, D. et al. Highly reliable ovonic threshold switch with TiN/GeTe/TiN structure. *Materials* **16**, 2066 (2023).
28. Velea, A. et al. Te-based chalcogenide materials for selector applications. *Sci. Rep.* **7**, 8103 (2017).
29. Cheng, H.-Y., Carta, F., Chien, W.-C., Lung, H.-L. & BrightSky, M. J. 3D cross-point phase-change memory for storage-class memory. *J. Phys. D Appl. Phys.* **52**, 473002 (2019).
30. Matsubayashi, D. et al. OTS Physics-based screening for environment-friendly selector materials. In *2022 International Electron Devices Meeting (IEDM)* 8.6.1–8.6.4 (IEEE, 2022).
31. Ravsher, T. et al. Polarity-dependent threshold voltage shift in ovonic threshold switches: challenges and opportunities. In *2021 IEEE International Electron Devices Meeting (IEDM)* 28.4.1–28.4.4 (IEEE, 2021).
32. Ravsher, T. et al. Enhanced performance and low-power capability of SiGeAsSe-GeSbTe 1S1R phase-change memory operated in bipolar mode. In *2022 IEEE Symposium on VLSI Technology and Circuits (VLSI Technology and Circuits)* 312–313 (IEEE, 2022).
33. Luo, M. & Wuttig, M. The dependence of crystal structure of te-based phase-change materials on the number of valence electrons. *Adv. Mater.* **16**, 439–443 (2004).
34. Li, H. & Robertson, J. Materials selection and mechanism of non-linear conduction in chalcogenide selector devices. *Sci. Rep.* **9**, 1867 (2019).
35. Oono, Y. & Puri, S. Study of phase-separation dynamics by use of cell dynamical systems. I. Modeling. *Phys. Rev. A* **38**, 434–453 (1988).
36. Clima, S. et al. Ovonic threshold switch chalcogenides: connecting the first-principles electronic structure to selector device parameters. *ACS Appl. Electron. Mater.* **5**, 461–469 (2023).
37. Lankhorst, M. H. R. Modelling glass transition temperatures of chalcogenide glasses. Applied to phase-change optical recording materials. *Mater. J. Non Cryst. Solids* **297**, 210–219 (2002).
38. Mihai, C. et al. Structural and optical properties of amorphous Si–Ge–Te thin films prepared by combinatorial sputtering. *Sci. Rep.* **11**, 11755 (2021).
39. Verdy, A. et al. Carbon electrode for Ge-Se-Sb based OTS selector for ultra low leakage current and outstanding endurance. In *2018 IEEE International Reliability Physics Symposium (IRPS)* 6D.4-1–6D.4-6 (IEEE, 2018).
40. Yamaguchi, M. et al. Understanding the cycling-dependent threshold voltage instability in OTS devices. In *2022 International Electron Devices Meeting (IEDM)* 5.1.1–5.1.4 (IEEE, 2022).
41. Hamilton, E. M. Variable range hopping in a non-uniform density of states. *Philos. Mag.* **26**, 1043–1045 (1972).
42. Ong, S. P., Wang, L., Kang, B. & Ceder, G. Li−Fe−P−O_2 phase diagram from first principles calculations. *Chem. Mater.* **20**, 1798–1807 (2008).
43. Cortes, C. & Vapnik, V. Support-vector networks. *Mach. Learn.* **20**, 273–297 (1995).
44. Pedregosa, F. et al. Scikit-learn: machine learning in python. *J. Mach. Learn. Res.* **12**, 2825–2830 (2011).
45. Noé, P. et al. Toward ultimate nonvolatile resistive memories: the mechanism behind ovonic threshold switching revealed. *Sci. Adv.* **6**, eaay2830 (2020).
46. Raty, J.-Y. & Noé, P. Ovonic threshold switching in Se-rich Ge_xSe_{1-x} glasses from an atomistic point of view: the crucial role of the metavalent bonding mechanism. *Phys. Status Solidi RRL* **14**, 1900581 (2020).
47. Pitochelli, A. R. & Audrieth, L. F. Concerning the existence of diphosphorus trisulfide. *J. Am. Chem. Soc.* **81**, 4458–4460 (1959).
48. Drabold, D. A. Topics in the theory of amorphous materials. *Eur. Phys. J. B* **68**, 1–21 (2009).
49. Kühne, T. D. et al. CP2K: an electronic structure and molecular dynamics software package - quickstep: efficient and accurate electronic structure calculations. *J. Chem. Phys.* **152**, 194103 (2020).
50. Perdew, J. P., Burke, K. & Ernzerhof, M. Generalized gradient approximation made simple. *Phys. Rev. Lett.* **77**, 3865–3868 (1996).
51. Goedecker, S., Teter, M. & Hutter, J. Separable dual-space Gaussian pseudopotentials. *Phys. Rev. B* **54**, 1703–1710 (1996).
52. Guidon, M., Hutter, J. & VandeVondele, J. Auxiliary density matrix methods for Hartree−Fock exchange calculations. *J. Chem. Theory Comput.* **6**, 2348–2364 (2010).
53. Clima, S. et al. Ovonic threshold-switching Ge_xSe_y chalcogenide materials: stoichiometry, trap nature, and material relaxation from first principles. *Phys. Status Solidi RRL* **14**, 1900672 (2020).
54. Chen, C., Ye, W., Zuo, Y., Zheng, C. & Ong, S. P. Graph networks as a universal machine learning framework for molecules and crystals. *Chem. Mater.* **31**, 3564–3572 (2019).
55. Jain, A. et al. Commentary: the materials project: a materials genome approach to accelerating materials innovation. *APL Mater.* **1**, 011002 (2013).

ACKNOWLEDGEMENTS

This work was carried out in the framework of the imec Core CMOS – Active Memory Program. T.R. acknowledges the support by Research Foundation – Flanders (FWO) for providing the funding via strategic basic research PhD fellowship (grant no. 1SD4721).

AUTHOR CONTRIBUTIONS

D.M. and S.C. both contributed equally to this work. G.S.K., S.C., and G.P. conceived the idea. S.C. and D.M. performed the ab initio simulations and theoretical data analysis. D.G. and R.D. fabricated the devices. T.R. and D.G. carried out experimental measurements. D.M. wrote the manuscript. All authors discussed the results and commented on/edited the manuscript.

COMPETING INTERESTS

The authors declare no competing interests.

ADDITIONAL INFORMATION

Supplementary information The online version contains supplementary material available at https://doi.org/10.1038/s41524-023-01043-2.

Correspondence and requests for materials should be addressed to Sergiu Clima.

Reprints and permission information is available at http://www.nature.com/reprints

Publisher's note Springer Nature remains neutral with regard to jurisdictional claims in published maps and institutional affiliations.

Open Access This article is licensed under a Creative Commons Attribution 4.0 International License, which permits use, sharing, adaptation, distribution and reproduction in any medium or format, as long as you give appropriate credit to the original author(s) and the source, provide a link to the Creative Commons license, and indicate if changes were made. The images or other third party material in this article are included in the article's Creative Commons license, unless indicated otherwise in a credit line to the material. If material is not included in the article's Creative Commons license and your intended use is not permitted by statutory regulation or exceeds the permitted use, you will need to obtain permission directly from the copyright holder. To view a copy of this license, visit http://creativecommons.org/licenses/by/4.0/.

© The Author(s) 2023